Composites Part B 161 (2019) 336–343

Contents lists available at ScienceDirect

Composites Part B

journal homepage: www.elsevier.com/locate/compositesb

Enhanced mechanical and arc erosion resistant properties by homogenously precipitated nanocrystalline fcc-Nb in the hierarchical W-Nb-Cu composite

Longchao Zhuo[a,b,*], Zhao Zhao[a], Zhicong Qin[a], Qiuyu Chen[a], Shuhua Liang[a,**], Xin Yang[a], Feng Wang[b]

[a] School of Materials Science and Engineering, Xi'an University of Technology, Xi'an, 710048, China
[b] National Center for Electron Microscopy in Beijing, School of Materials Science and Engineering, Tsinghua University, Beijing, 100084, China

ARTICLE INFO

Keywords:
Metal-matrix composites (MMCs)
Nanocrystalline
Microstructure
Electron microscopy

ABSTRACT

To achieve a combined enhancement of mechanical properties with improved arc erosion resistance, a novel strategy of two-step ball-milling and hot-press sintering under hydrogen for fabricating hierarchical W-Nb-Cu composite reinforced with in-situ nanocrystalline fcc-Nb was advocated. Characteristics including phase constituents, microstructure, mechanical properties and arc erosion behavior of the W-3 wt.%Nb-30 wt.%Cu composite have been systematically investigated. The crystal structure, grain size and phase distributions, as well as the specified surface work function of the three components of W, Cu and Nb were identified by XRD, TEM, EBSD experiments and DFT calculation. The enhanced mechanical properties were considered to result from the grain refinement of W and Cu with gradient micron to ultrafine scale, and the interfacially precipitated nanocrystalline fcc-Nb, which also acted as the first breakdown phase for effective dissipation of arc energies.

1. Introduction

The most resilient material developments required for fusion reactors beyond the International Thermonuclear Experimental Reactor (ITER) [1,2], at present the world's largest scientific-technical enterprise, are related to the in-vessel components of Tokamak fusion device [3]. Specifically, heat loads and plasma-induced erosion of the plasma-facing components (PFC) are the most concerned issues in thermonuclear fusion devices [4]. For the application of PFC, W-based materials, W-Cu laminated composites and W-Cu functionally graded composites are at present considered the most promising candidates over carbon/carbon fiber composites, beryllium or other refractory alloys [3,5–7]. Besides, W-Cu composites composed of immiscible components of W and Cu have attracted increasing attention and also been widely employed as high-voltage contact materials, solid rocket nozzle and other cutting-edge devices, owing to the combination of high conductive properties of Cu with outstanding arcing resistance and refractory characteristic of W [8,9]. As high-voltage electrical contact materials, W-Cu composites play an important role in connecting and breaking circuit. Under service conditions, they need to endure repeated mechanical force, and in the meantime, withstand high-temperature arc erosion. With the continuous development of switches to higher power voltage, larger capacity and miniaturization, the contact materials with better properties are urgently demanded [10].

Taking into consideration the quality and operational lifetime requirements, it is far from enough for the harsh application in W-Cu PFC fabrication nor for the severe usage in ultrahigh-voltage capacitor bank switch. Under this circumstance, substantial research is being undertaken massively to improve the performance of W-Cu composites through alloying, microstructure tailoring and compositing [11]. For instance, it has been reported that the W-Cu composites with addition of La_2O_3 exhibited highly improved arc erosion resistance [12,13]; however, the mechanical properties were dramatically deteriorated due to the grain boundary located La_2O_3 particles. Another attempt of replacement of W by WC to fabricate WC-Cu composite has also demonstrated its highly improved arc erosion resistance; nonetheless, a fatal weakness of poorly connected strength with Cu-based heat-sink alloys to form an integral material, gave rise to the final failure under service. Therefore, achieving the combined enhancement of arc erosion resistance with improved mechanical properties remains challenging.

Compared to the above ex-situ reinforcing composites, in-situ ones have been demonstrated to exhibit finer grain sizes, more homogenous distribution of reinforcements and cleaner interfaces, leading to enhanced mechanical properties [14,15]. On the other hand, the

* Corresponding author. School of Materials Science and Engineering, Xi'an University of Technology, Xi'an 710048, China.
** Corresponding author.
E-mail addresses: zhuolongchao@xaut.edu.cn (L. Zhuo), liangsh@xaut.edu.cn (S. Liang).

https://doi.org/10.1016/j.compositesb.2018.11.025
Received 23 July 2018; Received in revised form 31 October 2018; Accepted 3 November 2018
Available online 04 November 2018
1359-8368/

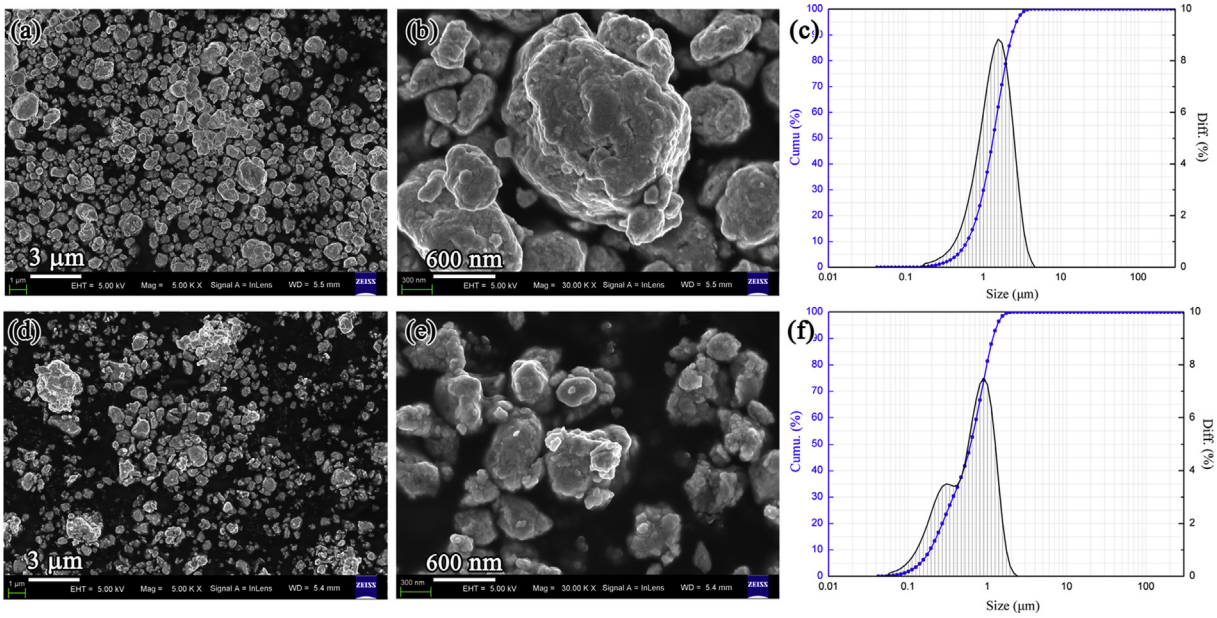

Fig. 1. SEM images and particle size distribution of the pre-milled W-4.29 wt.%Nb powders (a, b, c) and final-milled W-3 wt.%Nb-30 wt.%Cu powders (d, e, f). (Color figure online). (For interpretation of the references to color in this figure legend, the reader is referred to the Web version of this article.)

investigation of preparation of nanostructured materials has been the focus of recent scientific and technological investigation owing to their noteworthy and interesting characteristics as well as excellent applications in various fields [16,17], and different ways have been exploited for size controlled synthesis of nanostructured materials, including solid-state reaction, thermal decomposition, surface mechanical grinding, hydrogen plasma-metal reaction, cold rolling, and so on [18–24]. Herein, we present a hierarchical W-3 wt.%Nb-30 wt.%Cu composite reinforced with in-situ precipitated nanocrystalline fcc-Nb, through a novel strategy of two-step ball-milling and hot-press sintering under the atmosphere of reductive hydrogen. Characteristics including phase constituents, microstructure, mechanical properties and arc erosion behavior of the W-3 wt.%Nb-30 wt.%Cu composite have been systematically investigated and discussed. To the best of our knowledge, it is the first time that the calculation-predicted phase of fcc-Nb is experimentally confirmed in the present work. The results also exhibited a desired enhancement of mechanical properties with improved arc erosion resistance, which makes it useful for the development of PFC for fusion applications such as the blanket and divertor, or ultra-high-voltage circuit breaker usage.

2. Materials and methods

Commercially available tungsten powders (purity ≥ 99.9 wt.%, average size ~20 μm), niobium powders (purity ≥ 99.9 wt.%, average size ~25 μm) and copper powders (purity ≥ 99.9 wt.%, average size ~45 μm) were used as raw materials. First, mechanical alloying of nominal amount of W-4.29 wt.%Nb powders was performed in a high-energy ball-mill using a stainless steel container, with ball to powder weight ratio of 20:1 for milling duration of 20 h at a rolling speed of 400 r/min. Secondly, the pre-mixed W-Nb powders were further ball-milled with added Cu powders to obtain a final nominal amount of W-3 wt.% Nb-30 wt.%Cu, with ball to powder weight ratio of 4:1 for 4 h at a rolling speed of 400 r/min. Subsequently, the composite powders were pressed into green compacts with the dimension of φ 21 mm × 15 mm under the pressure of 340 MPa in a XTM-108-200T Hydraulic Press. Finally, the green compacts were sintered under the pressure of 30 MPa at 1240 °C for 40 min in hydrogen atmosphere followed by furnace cooling. The temperature precision of the sintering furnace is ± 5 °C. The metal ingots were machined and polished for later characterization.

The powder size distribution was obtained on a BT-2003 Laser Particle Sizer. The phase composition of the hot-press sintered specimen was investigated using a 7000S X-ray diffraction (XRD) instrument with Cu-*K*α radiation. The structure was also confirmed on a JEOL-3010 Transmission Electron Microscopy (TEM). The local crystallographic misorientation across the cross section of specimen (perpendicular to the hot-pressing axis and parallel to the arcing surface) was characterized by electron backscattering diffraction (EBSD) on a Zeiss Merlin SEM using the Oxford Nano-analysis EBSD camera and software under the acceleration voltage of 20 kV. Samples for EBSD were prepared by electric discharge machining, mechanical grinding and polishing, followed by a final vibratory polishing using colloidal silica on a MaterTex cloth for 3 h. The EBSD scan with a step size of 50 nm was used to obtain crystallographic misorientation distribution, grain morphology and phase map. Compressive properties were tested by using an Instron 5565 testing machine at a strain rate of $5.53 \times 10^{-4}\,s^{-1}$ at room temperature. The samples for compression were cut into a cylindrical shape with the dimension of 3 mm in diameter and 6 mm in height. The vacuum electrical breakdown tests were performed in a home-made vacuum arcing instrument under the voltage of 8 kV to simulate the arc erosion process, with a pure tungsten with needle shape as the anode and the tested sample as the cathode. The friction and wear experiments were conducted at the wear time of 180 min, the wear radius of 8 mm, the rotating speed of 80 r/min and the loading of 500 g on a HT-1000 Pin-on-Disk Tester with the wear pin and disk made of the present composite.

3. Results and discussion

Fig. 1 presents the SEM morphologies and particle size distribution of the pre-milled W-4.29 wt.%Nb (a, b, c) and final-milled W-3 wt.%Nb-30 wt.%Cu powders (d, e, f). It is indicated that the pre-milled W-4.29 wt.%Nb powders exhibit a median diameter of 1.55 μm. With more diffuse distribution and further refined particle size, the final-milled W-3 wt.%Nb-30 wt.%Cu powders exhibit a bimodal distribution of 0.30 μm and 0.90 μm. The bimodal distribution and the crystalline structure with high strain energy owning to severe cold working, would facilitate further powder rearrangement and densification during sintering.

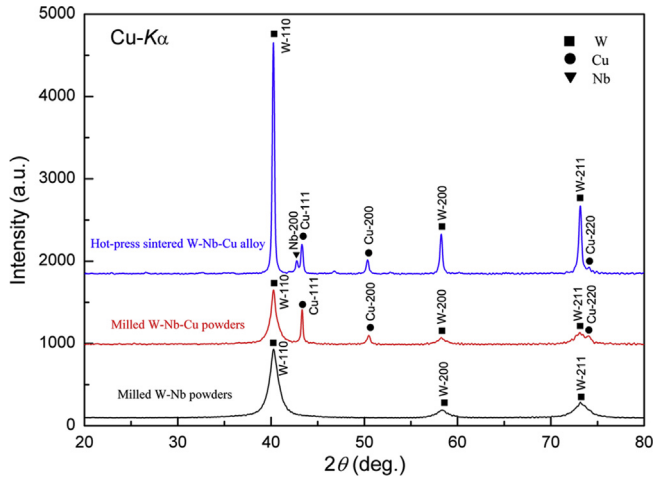

Fig. 2. XRD patterns of the pre-milled W-4.29 wt.%Nb powders and final-milled W-3 wt.%Nb-30 wt.%Cu powders, and as-sintered W-3 wt.%Nb-30 wt.%Cu composite. (Color figure online). (For interpretation of the references to color in this figure legend, the reader is referred to the Web version of this article.)

Furthermore, the pre-milled W-4.29 wt.%Nb and final-milled W-3 wt.%Nb-30 wt.%Cu powders, as well as the as-sintered W-3 wt.%Nb-30 wt.%Cu composite were tested by XRD to confirm the possible phase change after high-energy ball-milling or hot-press sintering. It can be seen from Fig. 2 that, for the pre-milled W-4.29 wt.%Nb powders (black line), the absence of diffraction peaks corresponding to Nb and the well-matched diffraction peaks of W reflections, indicated that the component Nb had been dissolved into W. However, due to the insensitivity of X-ray diffraction to minor amount of phases, it is speculated that some Nb could be present as segregation at grain boundaries or as sub-nanometric clusters. This has been proved by a displacement of 0.018° for Cu reflections, after further milling with Cu (red line). But one way or another, the two-step milled W-Nb-Cu powders are indexed to consist of only W and Cu, confirming the dissolution of Nb into them. Meanwhile, the diffraction peaks for W and Cu exhibited widened diffuse shape, indicating their decreased crystalline size. The mean crystallite size of the final milled W-Nb-Cu powders estimated by the Scherrer equation [16–19] resulted in a value of 74 nm for W and 93 nm for Cu. In contrast, after hot-press sintering, the phase composition of the resulted W-3 wt.%Nb-30 wt.%Cu composite were identified to include face-centered-cubic (fcc) structured Cu (space group: Fm-3m, International Center for Diffraction Data (ICDD) PDF: 70-3039), body-centered-cubic (bcc) structured W (space group: Im-3m, ICDD PDF: 04-0806) and fcc structured Nb (space group: Fm-3m, ICDD PDF: 88-2330). Notably, it should be marked that, the ICDD PDF data of 88–2330 for the phase of fcc-Nb is theoretically powder diffraction data predicted by Ab initio calculation [25] without any experimental evidence reported before. Here in the present W-3 wt.%Nb-30 wt.%Cu composite, the diffraction peak matching it in good agreement gives direct proof on this calculated phase. Moreover, the precipitated fcc-Nb here exhibited a strong preferred orientation of Nb-{200}. The driving force for the preferential precipitation of fcc-Nb is considered to be related to the loading state during hot-pressing at 1240 °C under the atmosphere of reductive hydrogen. However, due to its small quantities with relatively weak diffraction peak of this phase according to XRD, further vigorous and definite verifications of the newly experimentally reported phase of fcc-Nb were carried out by TEM and EBSD as shown in the following sections.

Fig. 3 (a) shows a typical bright-field TEM image for the W-3 wt.% Nb-30 wt.%Cu composite. The different contrast is caused not only by composition but also by crystallography. The corresponding selected-area diffraction (SAED) patterns definitely corroborate the phase existence of fcc-Nb, fcc-Cu and bcc-W. It can be seen in Fig. 3(b) taken from the smallest selected-area aperture that, besides the reflections given by fcc-Nb, there are also other unidentified weak spots, which indicates the overlapped precipitation with neighboring refined Cu or W. Comparatively, the SAED patterns of fcc-Cu and bcc-W are relatively pure and clean.

Rather than local-field TEM work, EBSD-based microstructure data is quantitatively adequate enough in that it captures statistically significant amount of grain information. Besides, the specimen for EBSD was prepared by surface mechanical polishing as described in the experimental section, eliminating ionic thinning effect for TEM confirmation. As shown in Fig. 4(a), the cross section of the as-sintered W-3 wt.%Nb-30 wt.%Cu composite was tilted at 70° for EBSD mapping. Fig. 4(b) shows the resulted Euler angle distributions with a resolution of 50 nm. The Hough transformation in Kikuchi pattern for identification of all phase constituents, consistent with the XRD and TEM results discussed earlier, further confirmed the existence of fcc-Nb, besides fcc-Cu and bcc-W. Meanwhile, ESBD provides an ideal solution to spatially correlated orientation by providing statistically significant data sets. As shown in Fig. 4(c), the inverse pole figure along Z (IPF-Z) for fcc-Nb from ND direction collected from EBSD data with intensities plotted in units of multiples of random (Fig. 4(c)) indicates that, the strong texture of < 001 > component was formed through hot-press sintering induced precipitation, which shows good accordance with the above XRD reflection from fcc-Nb.

The calculated grain size distribution (Fig. 4(d)) by EBSD statistical analysis reveals that, the grain size of fcc-Cu (ranging from 182 nm–1.99 μm) maintained an average value of 247 nm; the grain size of bcc-W (182 nm–1.23 μm) presented an average size of 266 nm, and the grain size of fcc-Nb (56 nm–357 nm) exhibited a mean value of 77 nm. The distinctly refined grain size distribution of fcc-Nb supported the confined precipitation of fcc-Nb from the neighboring matrix. It is well documented that the applied pressure during sintering would provide extra driving force for densification, promote nucleation and the in-situ precipitated particles may also act as the barriers of grain growth [26,27]. Therefore, the gradients in grain size, chemical composition, morphology and properties for the as-sintered W-3 wt.%Nb-30 wt.%Cu composite would result in good loading transfer due to the in-situ precipitation of the intact interface.

Fig. 4(e) presents the phase distribution map, with red corresponding to Cu, green to Nb and blue to W. Interestingly, almost all of the nanocrystalline fcc-Nb distributed homogenously between the phase boundaries of W and Cu, except for a little precipitation in the interior or the grain boundaries of Cu. The homogenously interfacial precipitated fcc-Nb created a specific local electronic environment and the properties would be tailored accordingly. Fig. 4(f) illustrates the local strain misorientation map, which was interpreted in terms of density of geometrically necessary dislocations (GND) [28] to present the local strain intensification. Accordingly, the large internal strain at the vicinity of red color where nanocrystalline fcc-Nb located, indicates a high density of GND. The GND has been demonstrated to accommodate the strain gradient under strain incompatibility [29,30]. Accordingly, with greatly increased grain boundary area and dislocation density, enhanced mechanical properties of the as-sintered W-3 wt.% Nb-30 wt.%Cu composite could be anticipated.

3.1. Mechanical behavior

As elaborated by Fig. 5(a), the W-3 wt.%Nb-30 wt.%Cu composite presents a highly reliable gigapascal flow or plateau stress of ~1020 MPa and a conspicuous plastic deformation stage with a uniform plasticity of ~8.6%. The gigapascal strength of the novel composite is significantly 85.9% higher than that of the commercial W-30 wt.%Cu composite [31]. This can be attributed to the homogenous distribution of the precipitated nanocrystalline fcc-Nb between the interphase of W and Cu, as well as the strong in-situ interfacial bonding which ensures the sufficient load transfer across the interface with

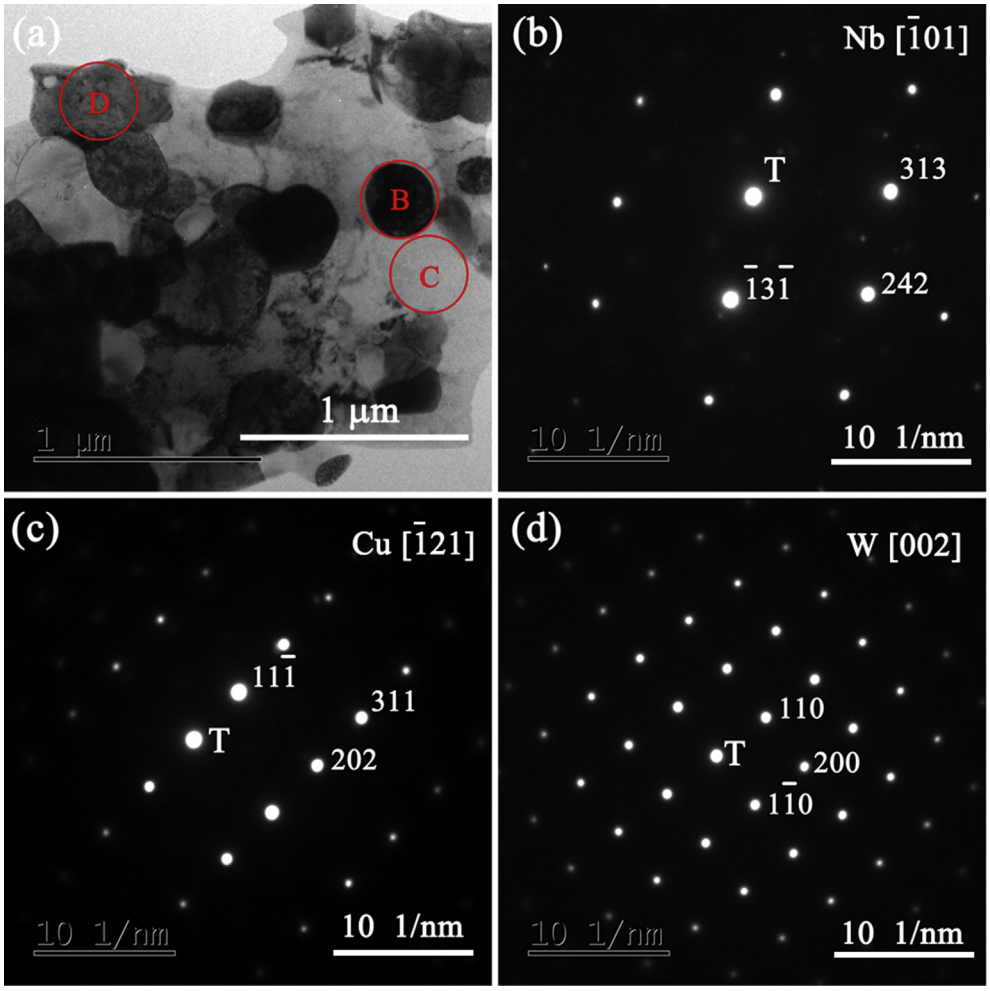

Fig. 3. Bright-field TEM image (a) and SAED patterns taken from the red circles of B, C and D were shown in respective (b), (c) and (d), for as-sintered W-3 wt.%Nb-30 wt.%Cu composite. (Color figure online). (For interpretation of the references to color in this figure legend, the reader is referred to the Web version of this article.)

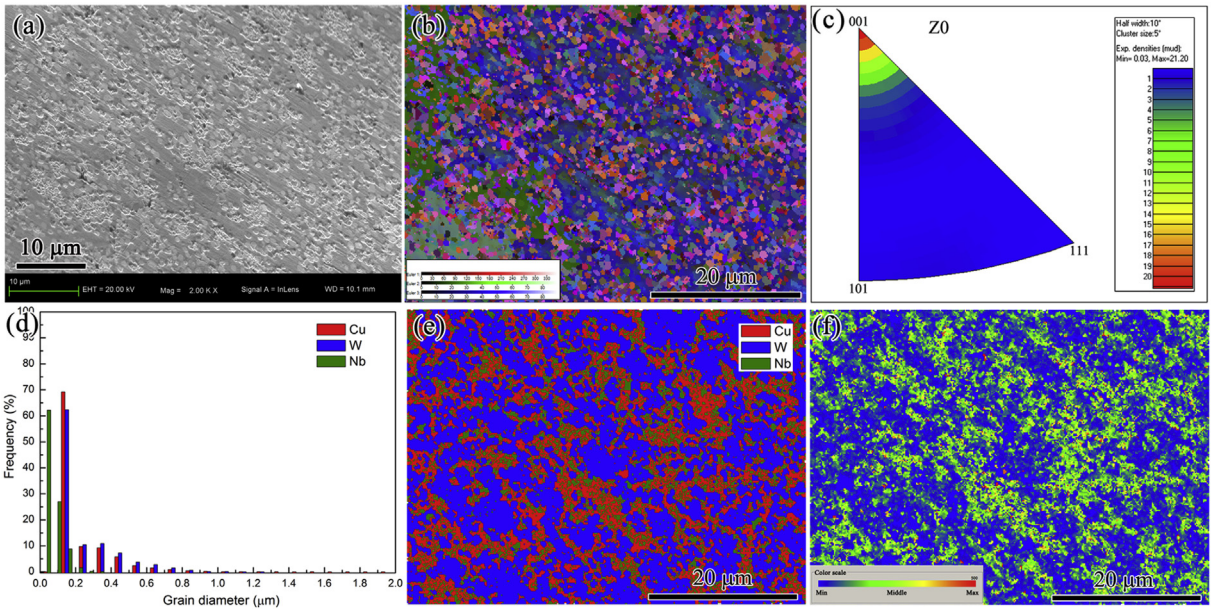

Fig. 4. SEM image of the cross section tilted at 70° for EBSD mapping (a), Euler angle distribution (b), IPF for fcc-Nb from ND direction (c), grain size distribution (d), phase map (e) and localized strain distribution (f), for as-sintered W-3 wt.%Nb-30 wt.%Cu composite. (Color figure online). (For interpretation of the references to color in this figure legend, the reader is referred to the Web version of this article.)

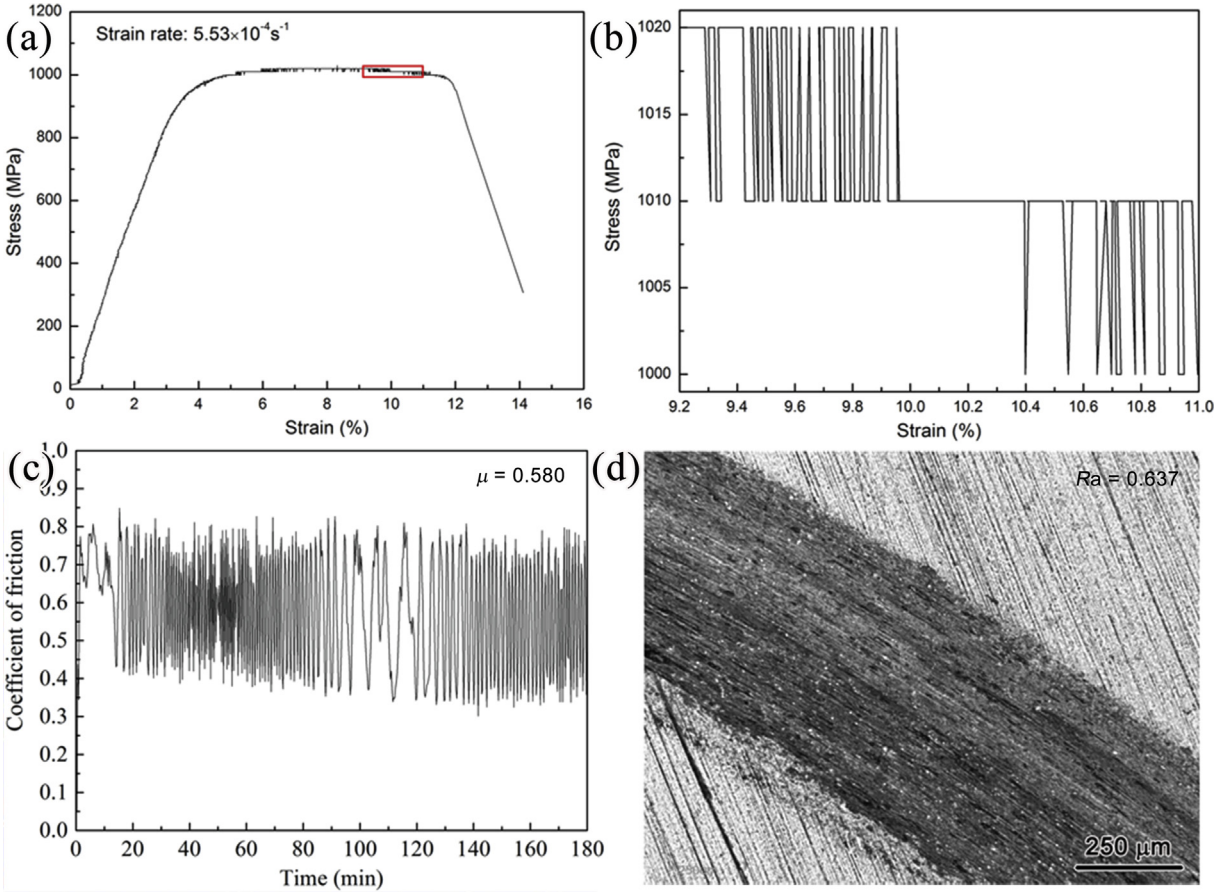

Fig. 5. Compressive stress-strain curve (a) with further magnified part (b) in the red rectangle as indicated in (a), as well as the friction coefficient curve (c) and the worn surface (d), for as-sintered W-3 wt.%Nb-30 wt.%Cu composite. (Color figure online). (For interpretation of the references to color in this figure legend, the reader is referred to the Web version of this article.)

dichotomy in strength for Cu and W. From the partially enlarged part of the plastic stage (Fig. 5(b)), the amplitudes of serrations with a value of 10 MPa clearly indicated a distinct serration feature of jerky/serrated flow, i.e. repeated and systematic fluctuations of loads during plastic deformation, which is usually considered to result from the restricted dislocation activities and the accumulated dislocations at interphases [32,33]. It can be thereby concluded that, during deformation, the GNDs as revealed by Fig. 4(f) may interact with mobile dislocations to increase their density in varying grains due to dislocation interaction and entanglement. The grain or phase boundaries near nanocrystalline fcc-Nb would act as effective high-angle barriers that impede the slip of dislocations. Therefore, the elastoplastic transition through load transfer and strain partitioning among gradient grains of various sizes, which is rationalized by the GND with separate regions that deform via different slip system combinations, strain amplitudes [20,23,34], resulted in a steady plasticity circumventing localization of strain.

It is commonly believed that the interface between W and Cu plays a significant role in determining the properties and lifetime of various W-Cu composites [35]. According to the microstructural analysis as revealed by Fig. 4(e and f), this novel composite with mixed grains of the three alternative components, with hierarchical characteristics both in grain size and strength matching as well as intact interface, would impart an improved wear resistant properties. For its service evaluation, friction and wear experiments of the W-3 wt.%Nb-30 wt.%Cu composite were also conducted. Fig. 5(c) exhibits the friction coefficient curve of the W-3 wt.%Nb-30 wt.%Cu composite. The composite proceeded into the stable stage of wear with a precedent initial wear of 16 min, and kept steady until 180 min. The average friction coefficient is determined to be 0.580, which is remarkably superior to the commercial W-Cu composite of 0.780 [36]. Fig. 5(d) illustrates the worn surfaces of the composite, without serious grooves or scratched concave-convex geometries with roughness (R_a) of 2.547 as detected for the commercial W-Cu composite [36]. The reduced R_a of 0.637 with shallow and thin scuffs are considered to be ascribed to the interfacially distributed nanocrystalline fcc-Nb, making the tungsten particles hard to fall off and inhibiting the degree of abrasive wear. The volume wear rate of the W-3 wt.%Nb-30 wt.%Cu composite was tested to be 7.29×10^{-7} mm^3 (N m)$^{-1}$, which reduced dramatically in comparison with the commercial W-30 wt.%Cu composite (4.18×10^{-5} mm^3 (N m)$^{-1}$) [31]. This is considered to result from the reservation of effective contact points and inhibition of pulling out of the tungsten particles between the pin and the disk during wear.

3.2. Arc erosion resistance

Recent investigations in Axially Symmetric Divertor Experiment (ASDEX) Upgrade show that erosion due to arcs has considered as the potential source for dust and for central plasma contamination. At the baffle of the inner divertor, up to 12% of the affected surface was eroded by uni-polar arcs [37]. On the other hand, in ultrahigh-voltage electric power system, the failure of contact materials has been established to derive from the excessive erosion of arc and rapid decrease of strength under high-frequency opening-closing environment [31]. Therefore, the evaluation of arc erosion resistance is crucially important for the reliability of the material used for nuclear fusion devices, also for the field of ultrahigh-voltage electric grid. Fig. 6 (a) presents the change of electrical breakdown strength with breakdown times for the as-sintered W-3 wt.%Nb-30 wt.%Cu composite. The average breakdown

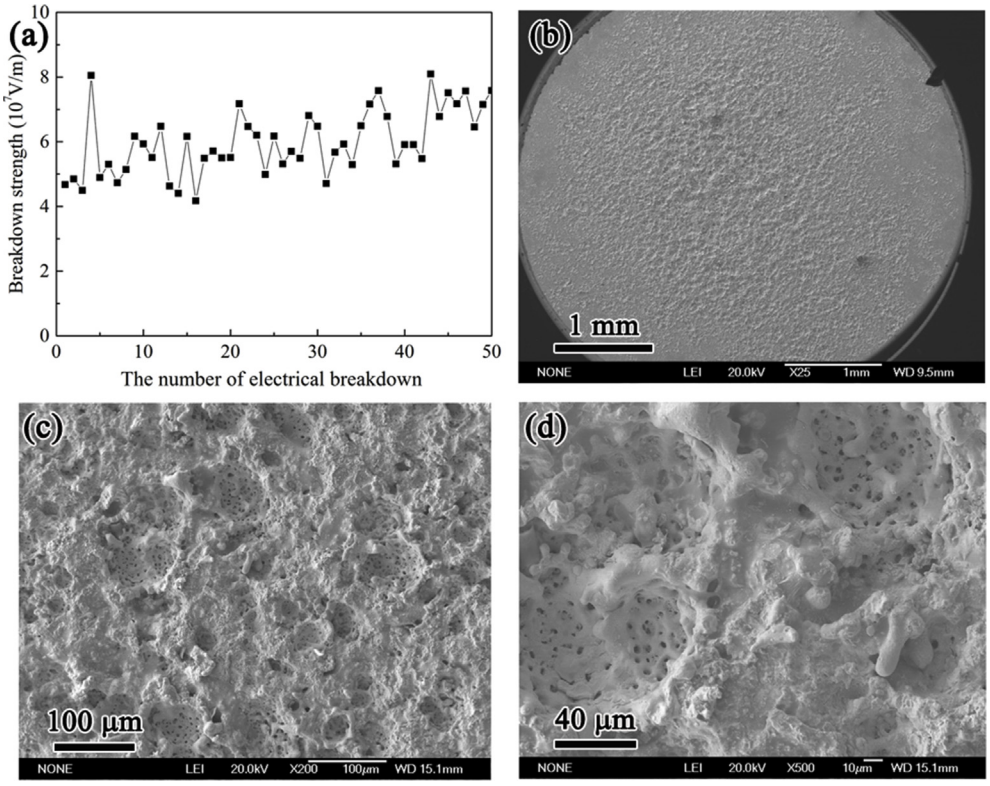

Fig. 6. The relationship between electrical breakdown strength and breakdown times (a) and surface morphologies (b) and further amplified SEM images (c, d) after breakdown for 50 times of as-sintered W-3 wt.%Nb-30 wt.%Cu composite.

strength of the composite was 5.98×10^7 V/m, which increased remarkably by 32.9% in comparison with that of the commercial W-Cu composite (4.50×10^7 V/m) [31], indicating its stability and reliability of the novel composite. Fig. 6(b–d) exhibit the surface morphologies of the composite after 50 times of electrical breakdown, indicating the behavior of complicated arc spots. Unlike the most serious arc erosion occurred in the central region underneath the anode tungsten tip where the microstructure became illegible and rough [36], for the present composite, the arc-affected region distributed more scattered and homogenously to almost the whole surface of the sample (Fig. 6(b)). What is more, it should be noted from Fig. 6(c and d) that multiple pores probably due to the evaporation of fcc-Nb formed at the eroded surface, which effectively distributed and carried the arc energies off the solid surface. To confirm the above speculation, the following density-functional theory (DFT) calculations were carried out.

As is commonly accepted, the electrons can be escaped from the material surface by tunneling effect if the electric field intensity of cathode reaches a critical value, leading to the occurrence of electrical breakdown and the arc discharging. The field emitted current density, J (A/m^2) obeys the formula derived by R.H. Fower and L. Nordherm [38].

$$J = \frac{1.541 \times 10^{-6} E^2}{\phi t^2(y)} \exp[-6.831 \times 10^9 \frac{\phi^{3/2}}{E} v(y)]$$

Where: E is the applied electric field strength (V/m), which is assumed to be constant; ϕ is the work function (eV); $y = 3.79 \times 10^{-4} E^{1/2} \phi^{-1}$; $t^2(y)$ and $v(y)$ can be taken as constants, $t^2(y) = 1.1$ and $v(y) = 0.95\text{-}y^2$.

As indicated by the above equation, the electron emission current remarkably increases with the decrease of the work function, and the different work functions of the components may result in notably different local arc properties including ignition preference, velocity and lifetime [39]. By the powerful quantum-mechanical approach for understanding or predicting crystal structures, and to elaborate the above experimental results of the dramatically enhanced arc erosion resistance, DFT calculations where the electron density is determined self-consistently from the solutions of the Kohn-Sham equations on periodic super-lattices were performed. In the analysis of the DFT results, particular attention has been addressed to the physical parameter of work function (ϕ). The DFT calculations were performed with the plane-wave pseudo potential method which allows to perform first-principles quantum mechanics calculations in the Cambridge Sequential Total Energy Package (CASTEP) software [40], where the generalized gradient approximation (GGA) in the form of Perdew-Berke-Ernzerhof function [41] was used exchange and correlation functional. The slab model for the calculation of work functions were constructed based on the optimized unit cells to obtain reliable results. Considering the preferred orientation formation indicated by XRD and EBSD, the dominant surfaces of W-(110), Cu-(111) and Nb-(200) were chosen for calculation. The corresponding atomic configurations are shown in the inset of Fig. 7(a–c). The vacuum slabs of 15 Å were used to avoid interactions between periodic images. A total number of 63 atoms was included for each slab model and geometry optimization of the bulk structure was performed to achieve a minimum system energy before work function calculations. The Brillouin zone was sampled by the k-points listed in Table 1 using the Monkhorst-Pack scheme. A self-consistent field (SCF) procedure (tolerance 5.0×10^{-7} eV/atom) was employed in conjunction with plane-wave basis sets of cutoff energy (E_{cutoff}) value listed in Table 1 using ultrasoft pseudopotentials [42] in reciprocal space.

Work function (ϕ) is the minimum energy required to remove an electron from the highest filled level in the Fermi distribution of a solid to vacuum outside the solid surface, which determines the arc erosion spot movement [43]. Fig. 7(a–c) show the charts of the electrostatic potential as a function of position along the surface normal, which Fermi energy (red line) and the vacuum energy (green line) level marked as two horizontal lines. The resulted work function values are also listed in Table 1, with previously reported values by other work in comparison [39,44]. The component of fcc-Nb with partially occupied

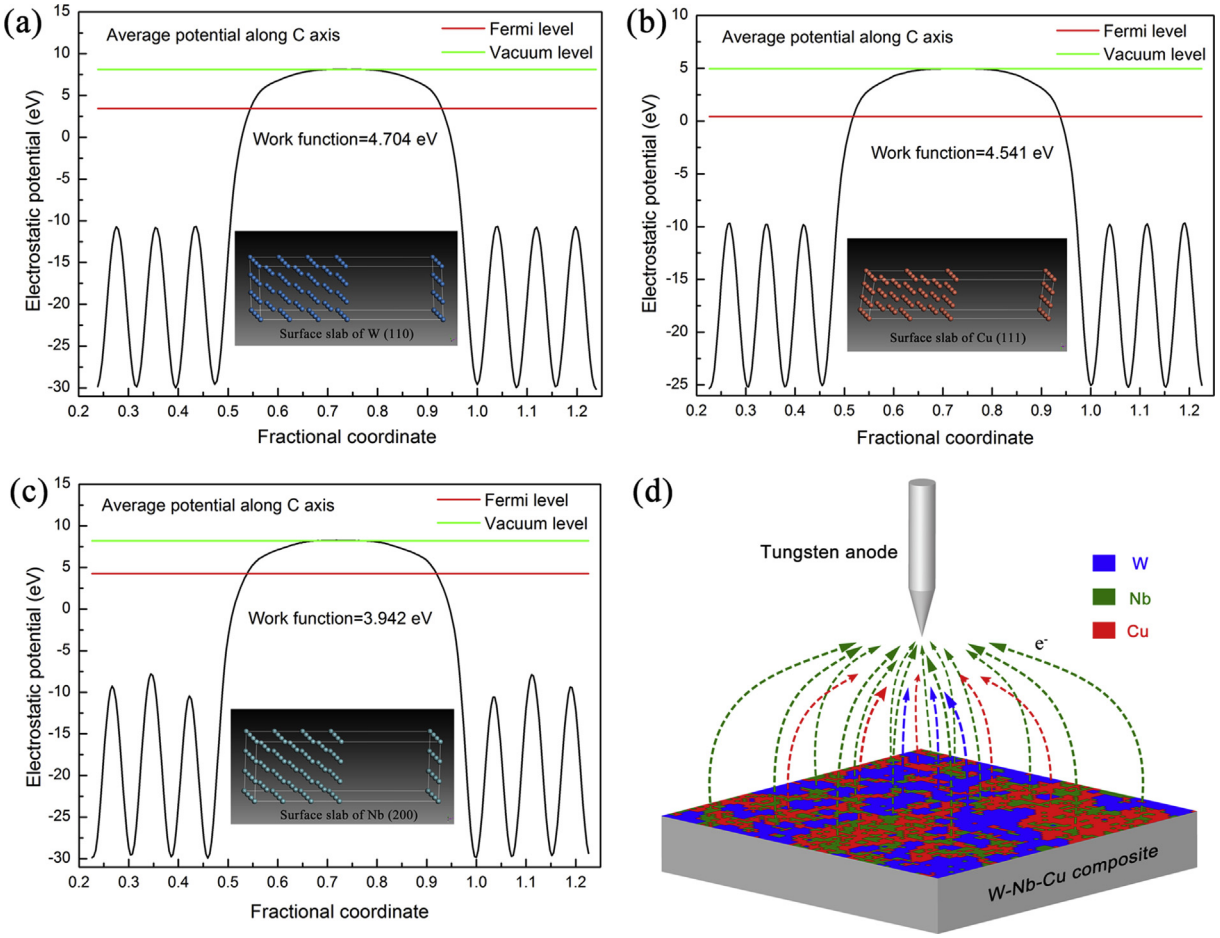

Fig. 7. Electrostatic potential distribution along the vertical direction (C axis) of the surfaces W-(110) (a), Cu-(111) (b) and Nb-(200) (c), as well as schematic diagram of electron transportation during electrical breakdown process of as-sintered W-Nb-Cu composite. (Color figure online). (For interpretation of the references to color in this figure legend, the reader is referred to the Web version of this article.)

Table 1
DFT calculation parameters and results of for components of W, Cu and Nb.

Component	Calculation parameters			This work	Other work
	Cleaved surface	k-points	E_{cutoff} (eV)	ϕ (eV)	ϕ (eV)
bcc-W	(110)	3 × 3 × 1	300	4.704	5.180 [44]
fcc-Cu	(111)	4 × 4 × 1	440	4.541	4.580 [39]
fcc-Nb	(200)	3 × 3 × 1	360	3.942	–

d-orbitals brought about opportunities for extraordinary electronic properties, exhibiting the lowest work function of 3.942 eV. Therefore, most of the cathode spots ignited preferentially on fcc-Nb, i.e. the first breakdown phase, as shown schematically in Fig. 7(d). Due to its homogenous distribution, fcc-Nb effectively dispersed the energy during arcing, making itself evaporated as observed in Fig. 6(b–d). In summary, as shown in Table 2 in comparison with other reported work [31,36,45,46], this novel composite reported here creates a new playground for performance improvement, such as mechanical property enhancement and arc erosion resistant design in W-Cu systems.

4. Conclusions

In this study, we advocate a strategy to achieve enhanced mechanical and arc erosion resistant properties, for which the W-3 wt.%Nb-30 wt.%Cu composite serves as a model system. The hierarchical W-3 wt.%Nb-30 wt.%Cu composite reinforced with homogenously precipitated nanocrystalline fcc-Nb was successfully prepared by a novel powder metallurgical method. The phase constituents, microstructure and mechanical properties as well as arc erosion behavior of the as-sintered sample were studied, and the following conclusions can be drawn:

(1) Complete mechanical alloying of the W-Nb-Cu powder mixtures consisting of only W and Cu phases was achieved after a two-step high-energy ball-milling. After hot-press sintering under the

Table 2
Property comparison of the W-3 wt.%Nb-30 wt.%Cu composite with other similar work.

Composites	Mechanical strength/MPa	Electrical breakdown strength/V·m^{-1}	Volume wear rate/(mm^3·(N·m)$^{-1}$)	References
W-3%Nb-30%Cu	1020	5.98×10^7	7.29×10^{-7}	This work
W@WC-30%Cu	679	5.05×10^7	8.12×10^{-6}	[31]
Ultrafine W-25%Cu	682	5.64×10^7	8.31×10^{-7}	[36,45]
W(W_f)-30%Cu	603	7.44×10^7	–	[46]
Commercial W-30%Cu	554	4.5×10^7	4.18×10^{-5}	[31]

pressure of 30 MPa at 1240 °C for 40 min in hydrogen atmosphere, a new phase of fcc-Nb was precipitated homogenously in the W-3 wt.%Nb-30 wt.%Cu composite.

(2) Diffraction techniques of XRD and SAED, as well as the Hough transformation in Kikuchi pattern for phase identification, have validated the existence of fcc-Nb for the first time by experiments, which was only predicted and reported previously by calculation. The in-situ nanocrystalline phase of fcc-Nb embedded in the W-3 wt.%Nb-30 wt.%Cu composite exhibited grain sizes ranging from 56 nm to 357 nm and a mean value of 77 nm.

(3) The W-3 wt.%Nb-30 wt.%Cu composite exhibited a highly enhanced compressive strength of ~1020 MPa (plateau-stress) with a plasticity of ~8.6%, and highly improved wear resistance. The enhanced mechanical properties were considered to result from the grain refinement of W and Cu with gradient micron to ultrafine scale, and the in-situ interfacially precipitated nanocrystalline fcc-Nb particles.

(4) The electrical breakdown strength of the W-3 wt.%Nb-30 wt.%Cu composite behaved a dramatically improved value of 5.98×10^7 V/m, which increased by 32.9% in comparison with that of the commercial W-30 wt.%Cu composite. Further DFT calculations revealed that the dramatically improved arc erosion behavior was ascribed to the homogenously precipitated fcc-Nb with the lowest work function value among the three constituent components, acting as the first breakdown phase for effective dissipation of the arc energies.

Acknowledgements

The authors would like to acknowledge the financial support of National Natural Science Foundation of China (Grant No. 51604223, 51504191and 51631002).

Appendix A. Supplementary data

Supplementary data to this article can be found online at https://doi.org/10.1016/j.compositesb.2018.11.025.

References

[1] Giancarli L, Chuyanov V, Abdou M, Akiba M, Hong BG, Lässer R, et al. Test blanket modules in ITER: an overview on proposed designs and required DEMO-relevant materials. J Nucl Mater 2007;367–370:1270–80.
[2] Casalegno V, Koppitz Th, Pintsuk G, Salvo M, Rizzo S, Perero S, et al. Proposal for a modified non-active brazing alloy for joining CFC composites to copper. Compos B Eng 2014;56:882–8.
[3] Knaster J, Moeslang A, Muroga T. Materials research for fusion. Nat Phys 2016;12:424–34.
[4] Hwangbo D, Kawaguchi S, Kajita S, Ohno N. Erosion of nanostructured tungsten by laser ablation, sputtering and arcing. Nucl Mater Energy 2017;12:386–91.
[5] Snead L, Ferraris M. Comprehensive nuclear materials. Elsevier; 2012. p. 583–620.
[6] Yang WL, Zhou LP, Peng K, Zhu JJ, Wan L. Effect of tungsten addition on thermal conductivity of graphite/copper composites. Compos B Eng 2013;55:1–4.
[7] Tejado E, Müller AV, You JH, Pastor JY. Evolution of mechanical performance with temperature of W/Cu and W/CuCrZr composites for fusion heat sink applications. Mater Sci Eng 2018;712:738–46.
[8] Lorentzen T, Clarke AP, Poulsen HF, Garbe S, Graafsma H. Local strain contours around inclusions in wire-drawn CuW composites. Compos Part A-Appl Sci 1997;28:667–74.
[9] Liu BB, Xie JX, Qu XH. Fabrication of W-Cu functionally graded materials with high density by particle size adjustment and solid state hot press. Compos Sci Technol 2008;68:1539–47.
[10] Seeger M. Perspectives on research on high voltage gas circuit breakers. Plasma Chem Plasma Process 2015;35:527–41.
[11] Ferroni F, Yi X, Arakawa K, Fitzgerald SP, Edmondson PD, Roberts SG. High temperature annealing of ion irradiated tungsten. Acta Mater 2015;90:380–93.
[12] Qian K, Liang S, Peng X, Wang X. In situ synthesis and electrical properties of CuW-La_2O_3 composites. Inter J Refract Met Hard Mater 2012;31:147–51.
[13] Li JW, Fang F, Wang Z, Zhang GS, Wei SZ, Xu LJ, et al. Microstructure and properties characterization of W-25Cu composite materials liquid-liquid doped with La_2O_3. Inter J Refract Met Hard Mater 2018;71:115–21.
[14] Luo SD, Li Q, Tian J, Wang C, Yan M, Schaffer GB, et al. Self-assembled, aligned TiC nanoplatelet-reinforced titanium composites with outstanding compressive properties. Scripta Mater 2013;69:29–32.
[15] Liu Z, Zhang DC, Gong LJ, Lin JG, Wen C. Microstructures and mechanical properties of in situ TiC-β-Ti-Nb composites with ultrafine grains fabricated by high-pressure sintering. Sci Rep 2018;8:9496.
[16] Beshkar F, Zinatloo-Ajabshir S, Bagheri S, Salavati-Niasari M. Novel preparation of highly photo-catalytically active copper chromite nanostructured material via a simple hydrothermal route. PLoS One 2017;12:0158549.
[17] Zinatloo-Ajabshir S, Salehi Z, Salavati-Niasari M. Green synthesis of $Dy_2Ce_2O_7$ ceramic nanostructures using juice of Punica granatum and their efficient application as photocatalytic degradation of organic contaminants under visible light. Ceram Int 2018;44:3873–83.
[18] Razi Fariba, Zinatloo-Ajabshir Sahar, Salavati-Niasari Masoud. Preparation, characterization and photocatalytic properties of Ag_2ZnI_4/AgI nanocomposites via a new simple hydrothermal approach. J Mol Liq 2017;225:645–51.
[19] Zinatloo-Ajabshir S, Morassaei MS, Salavati-Niasari M. $Nd_2Sn_2O_7$ nanostructures as highly efficient visible light photocatalyst: green synthesis using pomegranate juice and characterization. J Clean Prod 2018;198:11–8.
[20] Zhou X, Li XY, Lu K. Enhanced thermal stability of nanograined metals below a critical grain size. Science 2018;360:526–30.
[21] Zinatloo-Ajabshir S, Mortazavi-Derazkola S, Salavati-Niasari M. Nd_2O_3-SiO_2 nanocomposites: a simple sonochemical preparation, characterization and photocatalytic activity. Ultrason Sonochem 2018;42:171–82.
[22] Zinatloo-Ajabshir S, Salavati-Niasari M. Photo-catalytic degradation of erythrosine and eriochrome black T dyes using $Nd_2Zr_2O_7$ nanostructures prepared by a modified Pechini approach. Separ Purif Technol 2017;179:77–85.
[23] Yang MX, Yan DS, Yuan FP, Jiang P, Ma E, Wu XL. Dynamically reinforced heterogeneous grain structure prolongs ductility in a medium-entropy alloy with gigapascal yield strength. Proc Natl Acad Sci U S A 2018;115:7224–9.
[24] Zinatloo-Ajabshir S, Zinatloo-Ajabshir Z, Salavati-Niasari M, Bagheri S, Hamid SBA. Facile preparation of $Nd_2Zr_2O_7$-ZrO_2 nanocomposites as an effective photocatalyst via a new route. J Energy Chem 2017;26:315–23.
[25] Häglund J, Fernández Guillermet A, Grimvall G, Körling M. Theory of bonding in transition-metal carbides and nitrides. Phys Rev B 1993;48:11685–91.
[26] Ryum N, Hunderi O, Nes E. On grain boundary drag from second phase particles. Scripta Metall 1983;17:1281–3.
[27] Liao SC, Mayo WE, Pae KD. Theory of high pressure/low temperature sintering of bulk nanocrystalline TiO_2. Acta Mater 1997;45:4027–40.
[28] Kuhlmann-Wilsdorf D, Hansen N. Geometrically necessary, incidental and subgrain boundaries. Scripta Metall Mater 1991;25:1557–62.
[29] Wu XL, Jiang P, Chen L, Yuan FP, Zhu YT. Extraordinary strain hardening by gradient structure. Proc Natl Acad Sci USA 2014;111:7197–201.
[30] Huang CX, Wang YF, Ma XL, Yin S, Höppel HW, Göken M, et al Interface affected zone for optimal strength and ductility in heterogeneous laminate. Mater Today.10.1016/j/mattod. 2018.03.006.
[31] Zhang Q, Liang SH, Zhuo LC. Fabrication and properties of the W-30 wt%Cu gradient composite with W@WC core-shell structure. J Alloy Comp 2017;708:796–803.
[32] Zhang Y, Liu JP, Chen SY, Xie X, Liaw PK, Dahmen KA, et al. Serration and noise behaviors in materials. Prog Mater Sci 2017;90:358–60.
[33] Lu H, Li L, Huang XC, Li DY. An electron work function based mechanism for solid solution hardening. J Alloy Comp 2018;737:323–9.
[34] Hughes DA, Chrzan DC, Liu Q, Hansen N. Scaling of misorientation angle distributions. Phys Rev Lett 1998;81:4664–7.
[35] Ma GC, Fan JL, Gong HR. Mechanical behavior of Cu-W interface systems upon tensile loading from molecular dynamics simulations. Comput Mater Sci 2018;152:165–8.
[36] Zhang Q, Liang SH, Hou BQ, Zhuo LC. The effect of submicron-sized initial tungsten powders on microstructure and properties of infiltrated W-25 wt%Cu alloys. Inter J Refract Met Hard Mater 2016;59:87–92.
[37] Rohde V, Balden M. the ASDEX Upgrade Team. Arc erosion of full metal plasma facing components at the inner baffle region of ASDEX Upgrade. Nucl Mater Energy 2017;12:429–32.
[38] Fowler RH, Nordheim L. Electron emission in intense electric fields. Proc R Soc 1928;119:173–81.
[39] Wei X, Yu DM, Sun ZB, Yang ZM, Song XP, Ding BJ. Arc characteristics and microstructure evolution of W-Cu contacts during the vacuum breakdown. Vacuum 2014;107:83–9.
[40] Clark SJ, Segall MD, Pickard CJ, Hasnip PJ, Probert MJ, Refson K, et al. First principles methods using CASTEP. Zeitschrift fuer Kristallographie 2005;220:567–70.
[41] Perdew JP, Burke K, Ernzerhof M. Generalized gradient approximation made simple. Phys Rev Lett 1996;77:3865–8.
[42] Vanderbilt D. Soft self-consistent pseudopotentials in a generalized eigenvalue formalism. Phys Rev B 1990;41:7892–5.
[43] Lang ND, Kohn W. Theory of metal surfaces: work function. Phys Rev B 1971;3:1215–23.
[44] Leung TC, Kao CL, Su WS, Feng YJ, Chan CT. Relationship between surface dipole, work function and charge transfer: some exceptions to an established rule. Phys Rev B 2003;68. 195408-1-6.
[45] Zhang Q, Liang SH, Zhuo LC. Ultrafine-grained W-25 wt.%Cu composite with superior high-temperature characteristics. Mater Sci Technol 2017;33:2071–7.
[46] Zhuo LC, Zhang YH, Chen QY, Liang SH, Chen L, Zou JT. Fabrication and properties of the W-Cu composites reinforced with uncoated and nickel-coated tungsten fibers. Int J Refract Met Hard Mater 2018;71:175–80.